

Towards thrust vector control with a 3D steerable magnetic nozzle

IEPC-2015-414/ISTS-2015-b-414

*Presented at Joint Conference of 30th International Symposium on Space Technology and Science,
34th International Electric Propulsion Conference and 6th Nano-satellite Symposium
Hyogo-Kobe, Japan
July 4–10, 2015*

Mario Merino* and Eduardo Ahedo†

Equipo de Propulsión Espacial y Plasmas (EP2), Universidad Carlos III de Madrid, Leganés, Spain

A steerable magnetic nozzle concept is presented that enables contactless thrust vector control of a plasma jet without any moving parts. The concept represents a substantial simplification over current gimballed platforms, and requires only a small modification in plasma thrusters that already have a magnetic nozzle. A fully-magnetized plasma model is employed to characterize the 3D plasma expansion and the propulsive performance of the device. Results suggest that thrust deflections of 5–10 deg are easy to achieve. The differences, validity, and limitations of the fully- and partially-magnetized models are discussed in detail.

I. Introduction

MOST spacecraft using plasma thrusters require some thrust vector control (TVC) capability to modify the direction of the thrust force during the mission. TVC is needed to (i) compensate for misalignments with the center of mass of the spacecraft, which may occur in particular when this point shifts as the propellant is consumed, and (ii) unload the reaction wheels while firing the thrusters. An angular pointing range of 10 deg is sufficient for practically all applications. Current TVC solutions consist in mounting the thrusters on complex and heavy mechanical platforms with moving gimbals.^{1,2} As any other moving part, they are a delicate piece of equipment and may limit the reliability of the mission. Moreover, these pointing mechanisms introduce a number of problems of their own, such as the need to watch for flexible piping and connectors to the thruster, thermal control difficulties, or the damping of shocks and vibrations. Lastly, several of them only allow the rotation of the electric propulsion subassembly in one direction.

Magnetic nozzles³ (MN) are the ‘contactless’ acceleration stage of several next-generation thrusters, including the Helicon Plasma Thruster^{4,5} (HPT), the Electron-Cyclotron-Resonance thruster^{6,7} (ECRT) the Applied-field MPD⁸ (AF-MPD) and the VASIMR.⁹ In their usual design, they consist of an axisymmetric, convergent-divergent magnetic field that guides the expansion of a hot plasma into a supersonic jet. Inside the MN, the plasma gains axial kinetic energy at the expense of its internal energy, thanks to the self-consistent ambipolar electric field. The reaction to the magnetic forces that shape the plasma expansion are felt on the magnetic circuit of the thruster and generate ‘magnetic thrust’. In previous work^{10–12} we have characterized the 2D behaviour of the plasma in a divergent MN. The acceleration mechanisms, the ambipolar electric field, the development of electric currents in the plasma, and the generation of magnetic thrust were studied in Ref. 10. The problem of plasma detachment downstream, where the magnetic lines start to turn around, was discussed in detail in Ref. 11, and a clean detachment solution that respects the thrust-generation condition was found in Ref. 12. These results agree with existing laboratory experiments on the suitability of MNs to produce thrust in space propulsion applications.^{13–15}

Interestingly, new propulsive capabilities can be found when one considers a 3D MN. In this case, a non-axisymmetric convergent-divergent magnetic field guides and expands the plasma jet, but now it also

*Assistant Professor, Aerospace Engineering department, mario.merino@uc3m.es.

†Professor, Aerospace Engineering department, eduardo.ahedo@uc3m.es.

deflects it laterally. By controlling the 3D shape of the MN one could, in principle, create a *steerable magnetic nozzle* (SMN) to orient the plasma jet in any direction within a large angular range. This idea opens up the possibility of incorporating contactless thrust vector control (TVC) into the plasma thruster itself, without requiring any gimbaled platform or moving mechanical part. Such concept would therefore mean an important simplification of electric propulsion systems with respect to the current state of art.

One way to construct a SMN is to use a set of intertwined, tilted magnetic coils. By controlling the electric current that flows through each of these coils, it is possible to create an orientable 3D convergent-divergent magnetic field. This concept was recently presented by our group in Ref. 16, and has been termed VECMAN after Vector Magnetic Nozzle. The VECMAN design can be tailored to produce a deflection of 10, 15 deg or even larger angles, offering added flexibility to the mission, and it can be readily applied to any MN-based thruster, as well as other thrusters without magnetic field or with a nearly-axial magnetic field at the exit like the HEMPT^{17,18} and the DCFT.¹⁹

Magnetic deflection of plasma jets for space propulsion applications has been previously proposed using large external coils.²⁰ Also, additional magnetic circuits have been considered for magnetic TVC in Hall effect thrusters, to create an asymmetry in the internal magnetic field configuration that would cause a 3D plasma plume.²¹ One of the advantages of the VECMAN concept is that it only requires a small modification in the layout of the magnetic circuit of MN-enabled plasma thrusters, and does not have any moving part. As such, it does not increase substantially the thruster mass, or add any additional external component. Also, in VECMAN the TVC function takes place outside of the plasma source, which has its own magnetic field, and therefore it is possible to minimize the influence of the 3D magnetic configuration in the plasma generation process inside the thruster.

To preliminarily study MNs and SMNs it is essential to have simple, fast models that can estimate the propulsive performances of a device. By taking the full ion magnetization limit of our more complex DIMAGNO model,¹⁰ it is possible to derive a semianalytical model capable of tackling 2D and 3D expansions. Such a model needs to be first compared against the complete model to evaluate its range of validity, accuracy, and limitations.

The goal of this paper is to carry out a preliminary survey of the TVC capabilities of 3D MNs like the VECMAN configuration, as well as discuss the full-magnetization model. Section II introduces the VECMAN SMN and analyzes its magnetic field characteristics. Then, the fully-magnetized plasma expansion model is presented in Section III, which allows integrating the plasma flow in a quasi-1D manner. The model is first compared against the 2D partially-magnetized DIMAGNO model in Section IV, where its limitations and validity range are discussed. Then, the physics of the 3D plasma expansion are investigated with the fully-magnetized plasma model in Section V, where the TVC performance of VECMAN is tabulated for a representative set of cases. Lastly, in Section VI we gather the conclusions of this work and comment on the next steps.

II. VECMAN, steerable magnetic nozzle

VECMAN¹⁶ is a simple magnetic coil configuration that allows to create a SMN, in which the deflection and azimuth angle of the plasma jet can be controlled without any moving parts. The device can substitute any existing MN, and operate in axisymmetric or non-axisymmetric modes. Conceptually, it consists of N concentric coils tilted in some angle α with respect to the thruster axis. Each of them is precessed an angle $2\pi/N$ with respect to each other to create a symmetric device (Fig. 1). The current through each coil must be independently controllable. Physically, VECMAN may be constructed by winding simultaneously the N coils on a circular spool, resulting in a set of interwoven elliptic coils (Fig. 1 left), or by intertwining rigid circular coils of slightly different radii or slightly offset from the axis into that position (Fig. 1 right). To allow TVC in all directions, a minimum of 3 magnetic coils are used.

Using same-sign electric current on the coils allows to generate a MN whose axis can be oriented in any direction within a N -polygon, where the maximum deflection angle (at the vertices of this polygon) is α . The accessible angular space is depicted in Fig. 1 for $N = 3$ and 5, and $\alpha = 15$ deg. When all coils carry an identical number of ampere-turns, the axis of the MN coincides with the axis of the thruster (no deflection). The magnetic field in this case is near-axisymmetric, with small asymmetries becoming important only close to the metal of the coils. A larger α and a lower N increase the asymmetry and reduce the usable MN radius for the plasma. By using inverse electric currents through one or more coils it is possible to access orientations beyond the N -polygon, at the cost of a higher total current and field asymmetry.

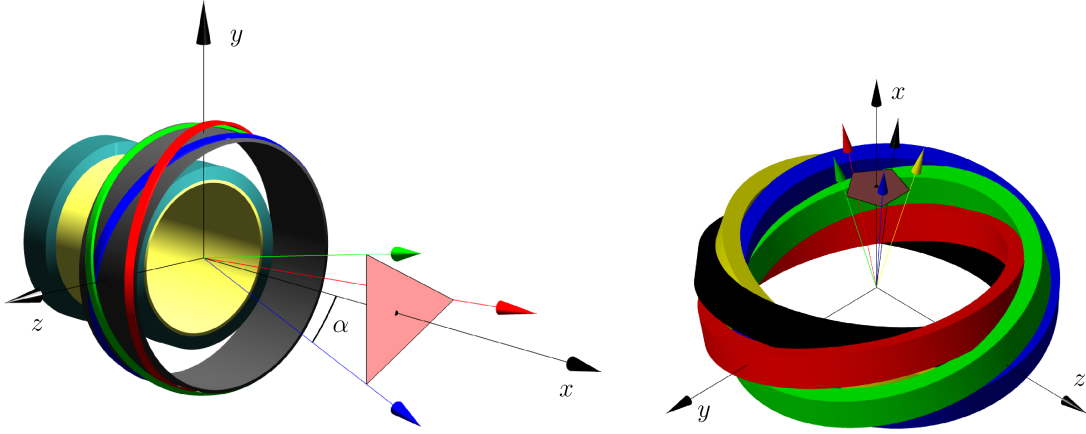


Figure 1. Sketch of the VECMAN steerable magnetic nozzle. *Left:* VECMAN set-up with a HPT-like plasma source and its solenoids (in yellow and beige), for $N = 3$ and $\alpha = 15$ deg. Three slightly elliptical coils (red, green blue) are wound simultaneously over a cylindrical support. The director vectors for each coil are displayed, to show that they are angularly equispaced. These vectors define the triangle (in red) of accessible angular deflections with same-sign currents on the coils. *Right:* VECMAN configuration with $N = 5$ and $\alpha = 15$, using intertwined circular coils slightly offset from the origin of coordinates (the plasma source is not shown). In this case, the same-sign currents accessible angular space is a pentagon.

The power needed to generate a MN of a given magnetic strength with VECMAN is roughly $1/\cos\alpha$ times larger than with a single coil of same radius and total mass. Thus, while increasing α extends the accessible angular space for deflection, it also increases the power budget of the thruster.

The VECMAN setup is placed near or at the exit plane of the plasma thruster. This way, it controls the shape and intensity of the magnetic field downstream, while the internal magnetic field is essentially governed by the rest of the thruster magnetic circuit (e.g. in a HPT, the internal field is generated by solenoids or permanent magnets). This allows to deflect the plasma jet without affecting substantially the internal plasma dynamics, therefore maintaining the internal efficiency of the device.

To model a complete magnetic field generator for the next Sections, we will consider the field created by a solenoid of radius $R_S = 2.5R$ and length $L_S = 8R$ that covers a fictitious plasma source of radius R . The VECMAN SMN to be studied is made of three circular point loops ($N = 3$) with radius $R_L = 6R$ and $\alpha = 15$ deg. The center of each coil is on the origin of coordinates. The director vector of the first of these loops is contained in the xz plane. Figure 2 shows this configuration and the magnetic field in an example deflection case. As it can be seen, the MN is deflected to one side, whereas the internal magnetic field remains almost unaffected by the SMN.

III. Fully-magnetized plasma expansion model

The study of the plasma flow in a SMN requires a 3D expansion model. A complete 3D model can be computationally expensive and lacks the physical insight of simpler models. In the interest of simplicity and clarity of the dominant aspects of the plasma expansion, this preliminary study of the SMN will consider the fully-magnetized limit of the two-fluid model presented in Ref. 10. As explained below, this limit yields several computational advantages that make it ideal for our present goals. The limit model is valuable by itself as a rapid tool for MN performance estimation.

The plasma tube in the SMN is assumed to have a clean lateral boundary to vacuum and to be composed of single-charged ions ($'i'$) and electrons ($'e'$). The plasma expansion is treated as quasineutral ($n_i \simeq n_e \equiv n$), collisionless, and low-beta (i.e., negligible induced magnetic field effects). Taking the typical orderings in a helicon plasma as a reference, we will neglect ion temperature with respect to electron temperature, $T_i \ll T_e$, and therefore describe ions as a cold species. Electron inertia is neglected with respect to ion inertia, $m_e \ll m_i$. Furthermore, we shall assume a simplified description of the electrons and model them as a Maxwellian, isotropic, isothermal species, so that $T_e = \text{const}$, with $T_e = p_e/n$. As seen in Ref. 22, some of these assumptions can be easily dropped and more complex thermodynamic models for ions and electrons

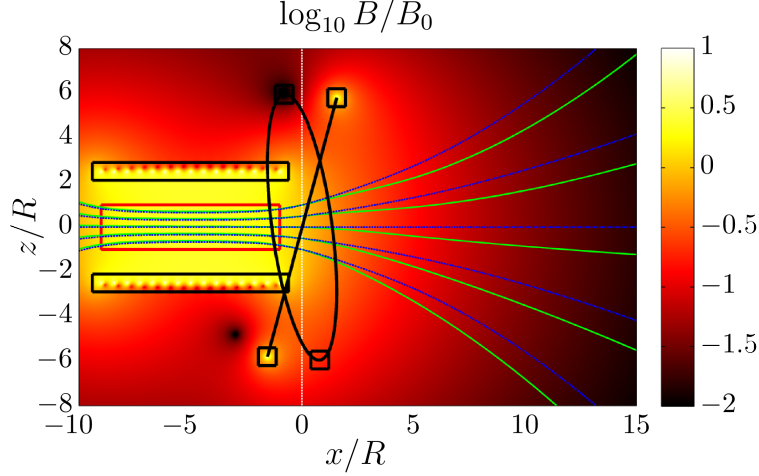


Figure 2. Magnetic field generator for the simulations of next sections. The generator is composed of a solenoid of 15 circular current loops of radius $R_S = 2.5R$, extending from $x = -9R$ to $x = -R$, and a VECMAN SMN made of circular coils with $N = 3$ and $\alpha = 15$ deg. The red box represents the ionization chamber of the thruster, which could be a helicon-like plasma source. The color map shows the magnetic field when the ampere-turn ratio between the solenoid and each of the three coils is $15 : 1 : 0 : 0$. Green lines show the magnetic streamlines that pass by the exit of the ionization chamber in this case. For comparison, the same streamlines in the symmetric configuration $15 : 0.33 : 0.33 : 0.33$ are shown blue.

can be adopted.

Under these hypotheses, the steady-state expansion can be described with the following continuity and momentum equations:

$$\nabla \cdot (n\mathbf{u}_i) = 0; \quad \nabla \cdot (n\mathbf{u}_e) = 0, \quad (1)$$

$$m_i (\mathbf{u}_i \cdot \nabla) \mathbf{u}_i = -e\nabla\phi + e\mathbf{u}_i \times \mathbf{B}, \quad (2)$$

$$0 = -T_e \nabla \ln n + e\nabla\phi - e\mathbf{u}_e \times \mathbf{B}, \quad (3)$$

where all symbols have the same conventional meaning as in Ref. 10. The model can be normalized with R , the initial plasma tube radius, m_i , e , and T_e . Likewise, we may normalize density with a reference value n_0 , e.g. its value at the origin. The isothermal sound velocity of the plasma $c_s = \sqrt{T_e/m_i}$ and the ion Mach number $M = u_i/c_s$ are defined as usual.

Both electrons and ions are assumed to be well magnetized. This requires, roughly, that $\hat{\Omega}_e \gg 1$ and $\hat{\Omega}_i \gg 1$ in the region under analysis. Here, $\hat{\Omega}_e = eBR/\sqrt{m_e T_e}$ and $\hat{\Omega}_i = eBR/\sqrt{m_i T_e}$ are the dimensionless electron and ion gyrofrequencies based on T_e . Note that the first ordering relation is equivalent to $\ell_e/R \ll 1$, with ℓ_e the electron Larmor radius.

When these conditions are met, an important simplification of the equations becomes possible. Ions and electrons move along magnetic lines with a velocity $O(c_s)$ except for a small drift velocity that scales as $O(T_e/eBR)$. According to the scalings above, this drift can be neglected in first approximation, so ion and electron streamlines coincide with magnetic streamlines. Hence, in the following we may write

$$\mathbf{u}_i = u_i \mathbf{1}_{\parallel}; \quad \mathbf{u}_e = u_e \mathbf{1}_{\parallel}, \quad (4)$$

where $\mathbf{1}_{\parallel} = \mathbf{B}/B$. Entering in Eqs. (1) with this approximation and using $\nabla \cdot \mathbf{B} = 0$, we immediately obtain

$$nu_i/B = G_i; \quad (5)$$

$$nu_e/B = G_e. \quad (6)$$

Projecting Eq. (2) and Eq. (3) along $\mathbf{1}_{\parallel}$ we recover the following ion and electron conservation laws on magnetic lines, respectively:

$$H_i = \frac{1}{2} m_i u_i^2 + e\phi, \quad (7)$$

$$H_e = T_e \ln n - e\phi. \quad (8)$$

In summary, we have 4 algebraic equations (Eqs. (5)–(8)) for 4 unknowns (u_i , u_e , n , ϕ), with 4 constants that can be calculated from the initial conditions. These can be given in an initial section of the plasma tube such as the plane $x = 0$. Given the external magnetic field, these equations can be readily solved to obtain the full plasma response.

Actually, the simplification $B \rightarrow \infty$ has reduced the 3D model to a 1D model per magnetic line: the evolution of the plasma properties along each line is completely independent from neighboring lines. Mathematically, if we consider the supersonic divergent side, the Mach cone that previously was a characteristic manifold of the problem has disappeared, leaving only the streamlines as characteristic lines. Therefore, the 3-hyperbolic problem degenerates into a 1-hyperbolic problem in this limit. Physically, this is due to the negligible role of the perpendicular pressure and electric field terms with respect to the magnetic ones when B is large; in the partially magnetized case, these pressure terms are responsible for carrying the information in the Mach directions. Observe that since the limit renders the problem 1-hyperbolic, it is easy to compute also the subsonic convergent part of the MN, a task that is inviable in 2D and 3D models based in the method of characteristics like the DIMAGNO code.¹⁰

IV. Fully-magnetized model vs DIMAGNO: validity and limitations

Clearly, the model we have derived is only strictly applicable to cases with very high values of $\hat{\Omega}_{i0}$, the ion gyrofrequency at the origin. Whereas electrons are readily magnetized with the usual magnetic strengths (200 G to 2 T), the heavier ions are typically only weakly magnetized: if we take typical HPT values like $R = 10$ cm and $T_e = 20$ eV for the plasma tube, we have $\hat{\Omega}_e > 1$ for $B > 10$ G roughly, while about 400 G are required to magnetize hydrogen ions, and 5000 G to magnetize xenon ions. Taking into account that B decreases with the nozzle area downstream and that area expansion ratios of 100 or more are common, very large magnetic strengths are therefore required at the throat to strictly maintain the full-magnetization limit until the MN turning point. Moreover, this is further aggravated when one considers that the relevant condition for the beginning of ion separation from the magnetic lines is actually¹² $(1 + \hat{\Omega}_i^2)/M^2 \ll 1$, and that M can increase from 1 at the throat to 5 or more near the turning point.¹⁰

Hence, it is clear that in the majority of practical devices, electrons are well-magnetized while ions are essentially unmagnetized, except perhaps in a small region near the MN throat. The question naturally arises whether we can use the $B \rightarrow \infty$ limit to study practical MN plasma expansions with lower $\hat{\Omega}_{i0}$ values. Also, we would like to quantify the error committed by this approximation in the calculation of plasma properties and propulsive performance figures. To this end, an axisymmetric MN expansion is simulated with both the $\hat{\Omega}_{i0} \gg 1$ model above and the 2D DIMAGNO model of Ref. 10 in the $\hat{\Omega}_{i0} \ll 1$ limit (i.e., no magnetic force on ions). Both models assume $\hat{\Omega}_e \gg 1$. The comparison of these two extremes will allow us to better understand their differences and infer certain conclusions on the range of validity and limitations of the full-magnetized model.

For the sake of illustration, our isothermal plasma is injected in the magnetic field of a single current loop of radius $R_L = 3.5R$. For this MN, the turning point is located at about $x = 16R$ and $y = 23R$. The following radial profile for density, potential and velocity is imposed at the magnetic throat ($x = 0$) between $y = 0$ and R :

$$n = n_0 \exp\left(-a \frac{y^2}{R^2}\right), \quad \phi = 0, \quad (9)$$

$$u_{xi} = u_{xe} = 1.01c_s, \quad u_{yi} = u_{ye} = 0, \quad (10)$$

where $a = 3 \ln 10$ is a parameter that controls the shape of the profile, and the 1.01 value is to ensure supersonic conditions for DIMAGNO. Moreover, for the DIMAGNO case, the azimuthal velocities are zero for ions, and a theta-pinch equilibrium is enforced for electrons,

$$u_{\theta e} = \frac{2T_e y a}{eBR}. \quad (11)$$

The simulation results are compared in Fig. 3. The major differences between the two ion magnetizations are as follows:

1. Ions begin to detach soon after the throat in the DIMAGNO simulation, and by $x = 10$ the separation in some of the mid-streamlines is already larger than $0.4R$. This separation is obviously missed in the

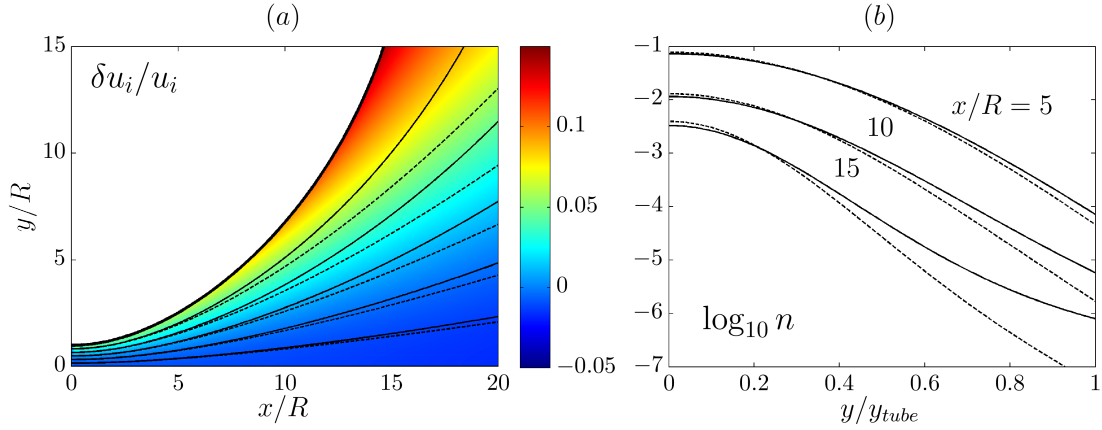


Figure 3. Comparison the full-magnetized model against the DIMAGNO model. Figure (a) shows the relative difference in ion velocity, $(u_i(\text{DIMAGNO}) - u_i(\text{Full-magnetized}))/u_i(\text{DIMAGNO})$. Ion streamlines have been drawn in solid line for the full-magnetized model and in dashed line for the DIMAGNO model. Figure (b) displays the radial density profile at various values of x . Here, y_{tube} is the radius of the plasma tube at each $x = \text{const}$ section. Solid lines are for the full-magnetized model and in dashed lines for the DIMAGNO model.

fully-magnetized model, where ion streamlines coincide with magnetic streamlines. Hence, this model is inadequate to study plasma detachment in actual partially-magnetized plasmas.

2. An ion velocity difference of about 15% occurs downstream at the periphery: the full-magnetized model yields a lower velocity there. In contrast, velocity at the axis is slightly larger.
3. As a consequence of point 1, the radial density profile is more spread out than in the DIMAGNO simulation. The full-magnetized model cannot recover this density focalization effect that takes place in partially-magnetized cases, as n is only a function of the relative drop in B along each streamline. As seen in Fig. 3 (b), the full-magnetized model slightly underestimates density at the axis, and largely overestimates density at the periphery. The effect continues to increase downstream, and at $x = 15R$ the difference can be about 2 orders of magnitude. Note that the expansion is not self-similar in either case over $x = \text{const}$ planes.
4. The ambipolar potential ϕ in the fully-magnetized limit is an inaccurate description of the potential in partially-magnetized cases, and using it for these cases can lead to large inconsistencies. The error in $e\phi/T_e$ is given by $\ln n$, so it can be inferred from Fig. 3 (b). When $\hat{\Omega}_i \ll 1$, the ion deflection task is performed primarily by the electric force (and in fact, it is insufficient to match the magnetic streamlines, and that is why ion separation occurs). In contrast, the deflection in the full-magnetized case is carried out by the magnetic forces alone (i.e., the products $eu_{\theta i}B$ and $-eu_{\theta e}B$). Radial density drop, potential drop, and ion separation are all coupled in the partially-magnetized case.
5. For the same reason, while $eu_{\theta i}B$ and $-eu_{\theta e}B$ are always finite, the electron and ion azimuthal velocities $u_{\theta i}$ and $u_{\theta e}$ go to zero when $B \rightarrow \infty$. In fact, we have supplanted the azimuthal and perpendicular momentum equations of the DIMAGNO model with the parallel flow condition. This renders the fully-magnetized model inadequate for the calculation of the key azimuthal plasma currents in a partially-magnetized case. These currents are the essential mechanism to create and transfer magnetic thrust back to the thruster; nonetheless, magnetic thrust can still be evaluated from a control volume integral of momentum flux, as done below.
6. In the fully-magnetized expansion no longitudinal electric currents develop. This is a consequence of the lack of ion separation. If the longitudinal currents are initially zero (i.e., when $G_e \equiv G_i$), they remain so everywhere. This brings up the local current ambipolarity (LCA) condition, so commonly invoked *a priori* in ambipolar diffusion models. The present comparison shows that in MNs, LCA is strictly only true in the $B \rightarrow \infty$ limit.

In spite of all these differences, the thrust F_x generated in the MN (seen as a function of the distance from the initial plane) is nearly insensitive to the magnetization degree up to the turning point. Also, it is seen that the $B \rightarrow \infty$ model yields a conservative value for all magnetizations of the divergence losses, here given by η_{plume} . These two functions are computed using a spherical control surface S of variable radius R_S with origin at $x = y = z = 0$, and integrating the relevant fluxes across them:

$$F_x(R_S) = \int_S n(T_e \mathbf{1}_x + m_i u_{xi} \mathbf{u}_i) \cdot d\boldsymbol{\sigma}, \quad (12)$$

$$\eta_{plume}(R_S) = \frac{\int_S n u_{xi}^2 \mathbf{u}_i \cdot d\boldsymbol{\sigma}}{\int_S n u_i^2 \mathbf{u}_i \cdot d\boldsymbol{\sigma}} \quad (13)$$

where $\mathbf{1}_x$ is the unit vector in the x direction and $d\boldsymbol{\sigma}$ is the differential area vector element over the spherical surface. $F_x(R_S)$ and $\eta_{plume}(R_S)$ for the simulations above are shown for different sphere radii in Fig. 4. Visibly, the thrust gain F_x/F_{x0} does not depend much on the value of $\hat{\Omega}_{i0}$; this suggests that the fully-magnetized model is a useful simple tool to estimate thrust from a MN in other cases.

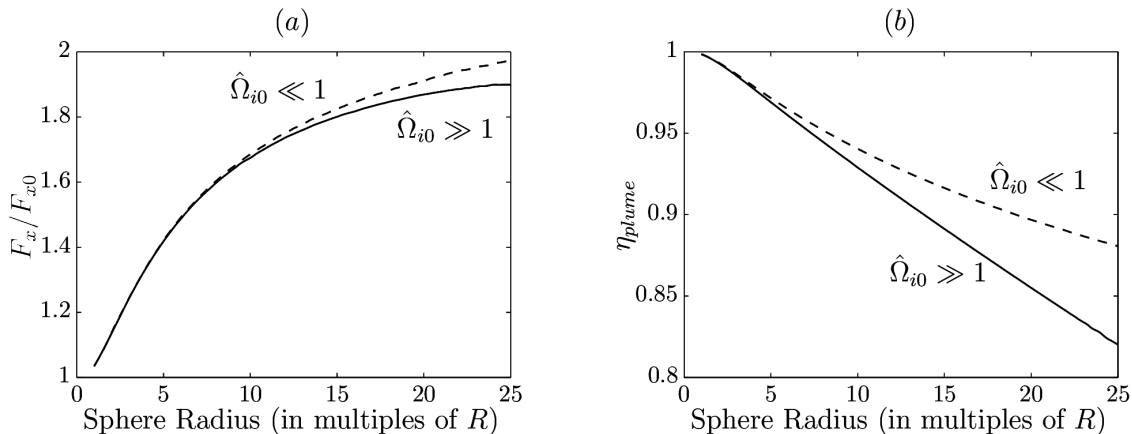


Figure 4. Thrust $F_x(R_S)/F_{x0}$ (a) and plume efficiency $\eta_{plume}(R_S)$ (b) with the fully-magnetized model (solid lines) and with DIMAGNO in the $\hat{\Omega}_{i0} \ll 1$ limit (dashed lines). F_{x0} is the total momentum flux at the magnetic throat plane, i.e., the initial thrust before the supersonic expansion. The two functions are computed using a sphere of radius R_S , starting at $R_S = 1.5R$. When the control sphere has radius 25 we are near the turning point of the MN (turning point takes place for a sphere radius $R_S \simeq 28R$).

Nonetheless, the higher the ion magnetization, the lower the thrust gain, as already concluded in the analysis of Ref. 10,11. The interest of the fully-magnetized limit here is that it provides the lower bound to the thrust gain for this plasma and arbitrary ion magnetization levels.

Regarding the plume divergence efficiency (Fig. 4 b), we observe that by the turning point (sphere of radius $\simeq 25R$), a difference of about 5% has developed between the zero- and full- ion magnetization cases. Again, the fully-magnetized model yields the lower limit, confirming its value as a simple, analytical model to conservatively estimate F_x and η_{plume} in axisymmetric MNs.

Clearly, the fully-magnetized model should not be extended beyond the turning point when approximating general magnetization cases. After this point, the strongly 2D character of the expansion and the large ion separation from the magnetic lines means that the error committed by the model increases. In fact, $F_x(R_S)$ begins to decrease about that point due to backflowing ions in the $\hat{\Omega}_{i0} \rightarrow \infty$ case, while it continues to increase monotonously but slowly for $\hat{\Omega}_{i0} \ll 1$ thanks to the successful plasma detachment.

While these results may encourage us to extend these conclusions to the 3D case right away, a word of caution is due. As discussed, partially-magnetized ions have a tendency to separate from the magnetic lines and continue in straight motion due to their large inertia. This can be expected to occur also in the 3D case. Moreover, the plasma-induced magnetic field (not considered in the above simulations) could act in a way that the effective magnetic deflection is reduced. While the effects of the full-magnetization assumption in the 3D case are not obvious, this suggests that the $B \rightarrow \infty$ model will overestimate the plasma deflection performance of a mild-strength SMN. Carefully checking the preliminary results of this paper with a 3D partially-magnetized model is left for future work.

In short, the fully-magnetized limit is a valuable tool for fast 2D preliminary estimations of thrust and plume efficiency, but lacks the necessary physical insight to study density focalization, ambipolar plasma potential, azimuthal currents and detachment in actual partially-magnetized MNs.

V. 3D expansion and thrust vector control in a SMN

To illustrate the fully-magnetized plasma expansion in the SMN, several simulations using the magnetic generator of Fig. 2 have been carried out with the previous model. A circular plasma tube of radius R is injected at $x = 0$ with a Gaussian initial density profile:

$$n = n_0 \exp\left(-a \frac{y^2 + z^2}{R^2}\right), \quad (14)$$

like before, we take $a = 3 \ln 10$ and $u_i = u_e = 1.01c_s$. The ratio of ampere-turns on the solenoid and each coil of the SMN is given in the second column of Table 1, for the different simulations. Those cases with weak VECMAN fields (O, A, B) do not disturb in practice the internal magnetic field of the plasma source (see Fig. 2). In the higher field cases (A', B'), VECMAN begins to cause a visible change in the inner magnetic field, but it still remains essentially axial everywhere in the plasma source. Simulation O has the turning point roughly at $x = 43R$, $y = z = 65R$, whereas the same simulation with 5 times more current on the VECMAN coils finds the turning point roughly at $x = 65R$, $y = z = 93R$.

Simulation	Ampere-turn ratios	F/F_0	ψ (deg)	θ (deg)	θ_B (deg)
O	15 : 0.33 : 0.33 : 0.33	1.44	–	0.00	0.00
A	15 : 1 : 0 : 0	1.44	–180.00	5.66	5.76
B	15 : 0.5 : 0.5 : 0	1.44	–120.00	2.86	2.91
A'	15 : 5 : 0 : 0	1.34	–180.00	11.06	11.24
B'	15 : 2.5 : 2.5 : 0	1.34	–120.00	5.61	5.70

Table 1. Thrust vector control simulations with VECMAN for Section V. Ampere-turn ratios are given as Solenoid : Coil 1 : Coil 2 : Coil 3. Simulation O is the symmetric configuration, used here for control. Simulations A and A' move the MN centerline toward one of the vertices of the triangle of Fig. 1. Simulations B and B' move it toward one edge. Simulations with a prime have a total current in the VECMAN coils 5 times stronger. The three next columns show the total thrust force F/F_0 , the azimuth angle of the thrust force $\psi = \arctan(F_y/F_z)$, and the polar angle $\theta = \arctan(\sqrt{F_y^2 + F_z^2}/F_x)$ on the control sphere with radius $R_S = 4.5R$ (early in the expansion). The last column shows the polar angle θ_B of the magnetic centerline for comparison.

The expansion of the fully-magnetized plasma follows the magnetic lines of the 3D MN. Figure 5 displays the plasma density in simulation A' . Clearly, the plasma jet moves to one side as dictated by the MN. The density distribution is no longer an exact circle downstream, but acquires some small ellipticity, with a lower density wing toward the direction of deflection. In the present model this is solely due to the differences in magnetic field strength along each streamline. For the same reason, the density maximum begins to separate slightly from the magnetic centerline downstream, but as it can be seen this separation is negligible in the case studied.

The three components of the thrust force function are evaluated in a similar way as the axial force $F_x(R_S)$ in the axisymmetric case (Eq. (12)): the total plasma momentum flux is integrated over different spherical surfaces with the center at the origin. The two lateral force components are:

$$F_y(R_S) = \int_S n(T_e \mathbf{1}_y + m_i u_{yi} \mathbf{u}_i) \cdot d\boldsymbol{\sigma}, \quad (15)$$

$$F_z(R_S) = \int_S n(T_e \mathbf{1}_z + m_i u_{zi} \mathbf{u}_i) \cdot d\boldsymbol{\sigma}. \quad (16)$$

The total force F , and its azimuthal and polar angles (ψ, θ) are shown in Table 1 for $R_S = 4.5R$, early in the expansion. A series of observations can be made from these results:

1. First, the magnitude of the total force F is essentially the same with and without deflection. In simulations A' and B' the thrust force at $R_S = 4.5R$ is lower due to the less-divergent MN, which

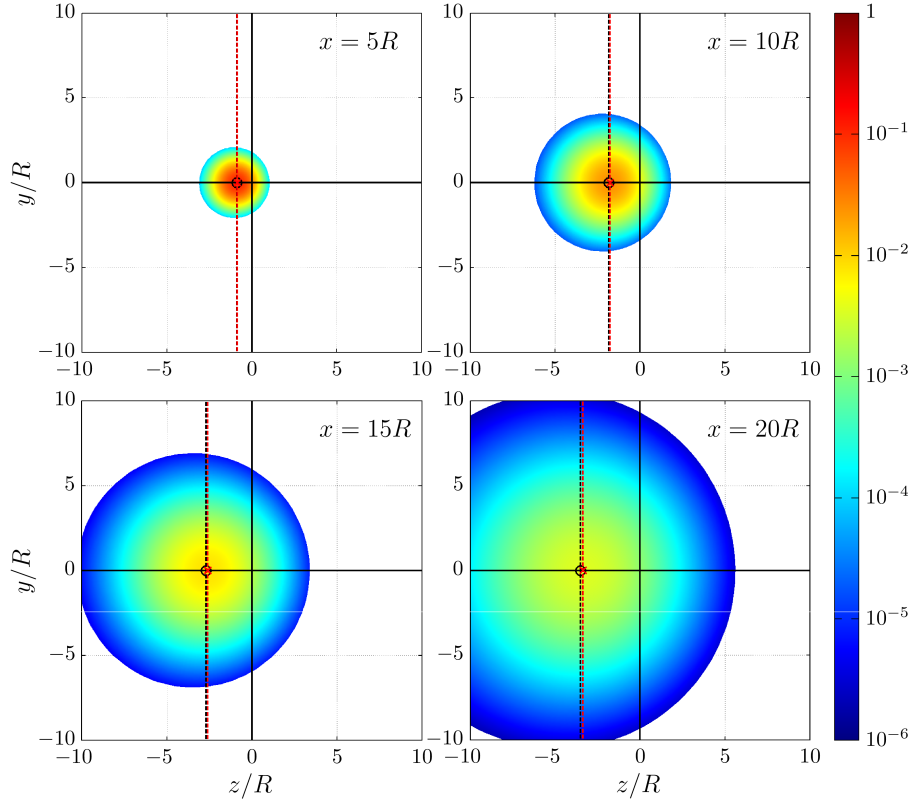


Figure 5. Density maps of the 3D plume n/n_0 at different axial $x = \text{const}$ sections for the A' simulation. The density map at $x = 0$ (not shown) is a perfectly symmetric circle of radius R and center on $y = z = 0$. The position of the central magnetic line that passes through the origin of coordinates is plotted as a black circle (on the black dashed line). The density maximum in each plane is located at the red cross (on the red dashed line).

occurs when the VECMAN coils carry more current. As explained in Ref. 10. this is actually a favorable feature: longer MNs have higher efficiency. A fairer comparison with the O , A and B simulations would consider the thrust force when the same area expansion ratio has been achieved.

2. Second, the polar angle θ of the thrust force is lower than the polar angle of the central magnetic line, θ_B , also shown in Table. 1 for comparison. This is due to the fact that the guiding magnetic lines experience an average deflection that is a bit lower than the deflection of the centerline, and the decrease of magnetic strength along them is not identical. This means that the bulk of the plasma density and momentum is not fully centered on each $x = \text{const}$ beam section, but tends to have slightly lower values in the direction of the deflection (as shown in Fig. 5 for n).
3. Third, as it could have been expected, the deflection is lower in simulations B and B' than in A and A' , as we are deflecting against one edge of the accessible angular space of Fig. 1 (the triangle in the sketch) rather than against one vertex. This causes the deflection of the centerline (and all other lines) to be lower in the B and B' simulations.
4. And fourth, increasing the strength of the SMN with respect to the solenoid increases the importance of the magnetic field of the former, causing a larger level of deflection of the magnetic centerline and consequently a higher deflection of the thrust force. In the limit of no solenoid current, the plasma would approach the limit deflection angle, which for A -type simulations is α , the tilt angle of the VECMAN coils (15 deg in our case), whereas it is $\arctan[\tan \alpha \sin(\pi/N)]$ ($\simeq 7.6$ deg) for B -type cases.

We conclude that the VECMAN SMN can deflect the plasma jet (and therefore the thrust force) in the fully-magnetized limit. If our conclusions from the 2D comparison of the fully- and partially-magnetized models (Section IV) can be extended to 3D case, then a similar deflection behavior to that of the $\hat{\Omega}_i \rightarrow \infty$ limit is to be expected for general magnetizations, at least before the expansion approaches the turning section of the SMN. However, due to the tendency of the supersonic ions to separate from the magnetic lines, it can be anticipated that our model probably yields an optimistic, higher-bound for the deflection in any particular configuration.

From these results we can also infer that higher α values allow for larger deflection angles. Likewise, increasing the number of independent coils N beyond three allows to have a more homogeneous and uniform accessible deflection angle in all directions. While it is not explored in this paper, using negative current through some of the coils allows deflecting the plasma to angles outside the direct accessible deflection space.

Finally, it has been shown that the SMN can work in combination with the internal magnetic fields of a HPT-like plasma thruster. As seen in Fig. 2, the SMN does not perturb substantially the geometry of the internal magnetic field when the relative ampere-turns are moderate. Naturally, larger coil currents (desirable from the viewpoint of larger deflection angles) can impact the magnetic configuration inside the plasma source.

VI. Conclusions

In this work a model for the fully-magnetized plasma expansion in a magnetic nozzle has been presented. The model is the mathematical limit of our DIMAGNO plasma model, and allows analytical computation of the propulsive performances of 2D and 3D magnetic nozzles. A comparison between this limit model and the more general partially-magnetized model has been carried out for the axisymmetric case. The main conclusions of this analysis are that the fully-magnetized model can be used to yield sensible, conservative estimations of the thrust and plume efficiency of the magnetic nozzle up to the turning point regardless of the ion magnetization level. The model cannot be used however to study the plasma detachment, radial density focalization, ambipolar electric field, and azimuthal plasma currents in partially-magnetized cases; these aspects require a partially-magnetized model like DIMAGNO.

The concept of a steerable magnetic nozzle that can deflect the plasma jet in arbitrary directions in a contactless manner has been introduced. The VECMAN steerable magnetic nozzle is a simple realization of this idea without any mechanical moving parts, where the direction of the thrust force can be controlled by varying the electric current through several intertwined coils that can easily substitute an existing magnetic nozzle. This form of contactless magnetic deflection represents an interesting alternative to the existing gimbaled platforms that are used to reorient the whole plasma thruster.

The thrust vector control performance of VECMAN has been evaluated in the fully-magnetized case. The simulation results show that the expected thrust deflection is obtained, proving that the device is a simple means to integrate the required thrust vectoring capabilities directly in the plasma thruster. Maximum deflection is sensitive to the tilt angle of the magnetic nozzle coils, the number of coils used, and the relative intensity of the currents through them and other parts of the magnetic circuit of the thruster. An ample range of currents exists where internal magnetic fields are essentially unperturbed by the 3D magnetic nozzle.

Future work shall focus on improving the range of validity of the 3D plasma model by relaxing the full magnetization condition and including other effects (induced magnetic field, etc.). An important question to answer is what is the minimum ion magnetization strength, if any, required to deflect the plasma beam. Understanding the behavior of the plasma electric currents in the 3D partially-magnetized expansion is also a crucial aspect. A more complete characterization of VECMAN deflection capabilities and thruster interaction needs to be carried out, too. Lastly, the construction of a first VECMAN prototype that can be used to validate these theoretical results in combination with a representative plasma source is planned for the coming year.

Acknowledgments

This work has been supported by the Spanish R&D National Plan, grant number ESP2013-41052-P.

References

- ¹Kugelberg, J., Bodin, P., Persson, S., and Rathsman, P., "Accommodating electric propulsion on SMART-1," *Acta Astronautica*, Vol. 55, No. 2, 2004, pp. 121–130.
- ²Wood, B., Gasparini, E., Buff, W., and Skulicz, A., "The development of a multi-purpose thruster orientation mechanism," Vol. 320, 2011, p. 930.
- ³Andersen, S., Jensen, V., Nielsen, P., and D'Angelo, N., "Continuous Supersonic Plasma Wind Tunnel," *Phys. Fluids*, Vol. 12, 1969, pp. 557–560.
- ⁴Batishchev, O., "Minihelicon Plasma Thruster," *IEEE Transaction on Plasma Science*, Vol. 37, 2009, pp. 1563–1571.
- ⁵Merino, M., Navarro, J., Casado, S., Ahedo, E., Gómez, V., Ruiz, M., Bosch, E., and del Amo, J. G., "Design and development of a 1kW-class helicon antenna thruster," *34th International Electric Propulsion Conference*, No. IEPC-2015-297, Electric Rocket Propulsion Society, Fairview Park, OH, 2015.
- ⁶Sercel, J. C., "Electron-cyclotron-resonance (ECR) plasma acceleration," *AIAA 19th Fluid Dynamics, Plasma Dynamics and Lasers Conference*, 1987.
- ⁷Jarrige, J., Elias, P.-Q., Cannat, F., and Packan, D., "Characterization of a coaxial ECR plasma thruster," *44th AIAA Plasmadynamics and Lasers Conference, San Diego*, 2013.
- ⁸Krülle, G., Auweter-Kurtz, M., and Sasoh, A., "Technology and application aspects of applied field magnetoplasma dynamic propulsion," *J. Propulsion and Power*, Vol. 14, 1998, pp. 754–763.
- ⁹Diaz, C., "The VASIMR rocket," *Scientific American*, Vol. 283, No. 5, 2000, pp. 90–97.
- ¹⁰Ahedo, E. and Merino, M., "Two-dimensional supersonic plasma acceleration in a magnetic nozzle," *Physics of Plasmas*, Vol. 17, 2010, pp. 073501.
- ¹¹Ahedo, E. and Merino, M., "On plasma detachment in propulsive magnetic nozzles," *Physics of Plasmas*, Vol. 18, 2011, pp. 053504.
- ¹²Merino, M. and Ahedo, E., "Plasma detachment in a propulsive magnetic nozzle via ion demagnetization," *Plasma Sources Science and Technology*, Vol. 23, 2014, pp. 032001.
- ¹³Schuettpelz, B., Li, Z., and Cassibry, J., "Plume Diagnostics Supporting Magnetic Nozzle Plasma Detachment Demonstration Experiment," *42nd AIAA/ASME/SAE/ASEE Joint Propulsion Conference & Exhibit*, 2006.
- ¹⁴Longmier, B., Bering, E., Carter, M., Cassady, L., Chancery, W., Díaz, F., Glover, T., Hershkowitz, N., Ilin, A., McCaskill, G., et al., "Ambipolar ion acceleration in an expanding magnetic nozzle," *Plasma Sources Science and Technology*, Vol. 20, 2011, pp. 015007.
- ¹⁵Olsen, C., Ballenger, M., Carter, M., Chang Diaz, F., Giambusso, M., Glover, T., Ilin, A., Squire, J., Longmier, B., Bering, E., and Cloutier, P., "Investigation of Plasma Detachment From a Magnetic Nozzle in the Plume of the VX-200 Magnetoplasma Thruster," *Plasma Science, IEEE Transactions on*, Vol. 43, No. 1, Jan 2015, pp. 252–268.
- ¹⁶Merino, M. and Ahedo, E., "Sistema sin partes móviles ni electrodos y procedimiento para vectorizar el empuje en motores espaciales de plasma," 2013, submitted to the Spanish Patent Office, Patent no. P201331790.
- ¹⁷Kornfeld, G., Koch, N., and Coustou, G., "First Test Results of the HEMP thruster concept," *Proceedings of the 28th International Electric Propulsion Conference*, 2003.
- ¹⁸Koch, K. and Schirra, M., "The HEMPT Concept - A Survey on Theoretical Considerations and Experimental Evidences," *32nd International Electric Propulsion Conference*, No. IEPC-2011-236, IEPC-2011-236, Wiesbaden, Germany, 2011.
- ¹⁹Courtney, D. and Martínez-Sánchez, M., "Diverging Cusped-Field Hall Thruster," *30th International Electric Propulsion Conference, Florence, Italy*, IEPC-2007-39, 2007.
- ²⁰Cox, W., Charles, C., Boswell, R., Laine, R., and Perren, M., "Magnetic Ion Beam Deflection in the Helicon Double-Layer Thruster," *Journal of propulsion and power*, Vol. 26, No. 5, 2010, pp. 1045–1052.

²¹Duchemin, O., Prioul, M., Iland, H., Banetta, S., Vicini, A., Garrigues, L., Rigollet, R., and Estublier, D., “Development of a Prototype Thrust Steering Device for Hall-Effect Thrusters,” *4th International Spacecraft Propulsion Conference*, Vol. 555, 2004, p. 42.

²²Merino, M. and Ahedo, E., “Influence of Electron and Ion Thermodynamics on the Magnetic Nozzle Plasma Expansion,” *IEEE Transactions on Plasma Science*, Vol. 43, No. 1, Jan 2015, pp. 244–251.